Baroclinic Wave Packets in Models and Observations

SUKYOUNG LEE*

Atmospheric and Oceanic Science Program, Princeton University, Princeton, New Jersey

ISAAC M. HELD

Geophysical Fluid Dynamics Laboratory/NOAA, Princeton University, Princeton, New Jersey

(Manuscript received 10 February 1992, in final form 18 August 1992)

ABSTRACT

Coherent baroclinic wave packets are present in the Southern Hemisphere, most clearly in the summer season. These coherent packets are also found in a hierarchy of models of nonlinear baroclinic instability—a two-layer quasigeostrophic (QG) model on a β-plane, a two-level primitive equation (PE) model, and a general circulation model. The flows are chaotic, but the packet itself can remain remarkably coherent, despite the complex evolution of the flow within the packet. In both QG and PE models, the packets become more robust as the supercriticality of the flow is reduced. In both models and the observations, the packets move with a group velocity that is greater than the phase speed of the individual disturbances, so that these disturbances exhibit downstream development. The structure of the baroclinic waves in the packet as a function of longitude resembles the life cycles of sinusoidal baroclinic waves as a function of time. More than one packet can exist in the domain at the same time. In the QG model, the number of packets increases in a systematic way as the length of the channel increases.

1. Introduction

The Southern Hemisphere (SH) circulation provides an important proving ground for theories and models of finite amplitude baroclinic instability. It is useful to study the development and organization of baroclinic eddies without the complexity introduced by the large planetary waves and localized storm tracks of the Northern Hemisphere (NH). In this paper we focus on the coherent baroclinic wave packets into which eddies are organized in the SH, particularly in summer, and show that such packets form spontaneously in a variety of models.

Randel and Stanford (1985) describe a particularly simple form of eddy development in the SH summer, in which a single zonal harmonic dominates the flow, and in which there is near simultaneous growth of a series of disturbances around a latitude circle. The waves grow due to baroclinic energy conversion and then decay due to the barotropic transfer of energy to the zonal flow. The calculations of Simmons and Hoskins (1978) with a primitive equation model on the sphere, initialized with the most unstable normal mode, mimic this life cycle remarkably well. This qualitative behavior can also be seen in the simplest two-layer quasigeostrophic model of an unstable westerly jet, if one initializes the flow with an unstable normal mode (Feldstein and Held 1989; Feldstein 1991). However, this modal form of development is relatively rare, both in the atmosphere and in atmospheric models.

More typically, the amplitude of baroclinic waves is strongly modulated in longitude, by an envelope or packet of wave activity. As described in the following, this envelope can propagate coherently, retaining its shape, while the disturbances within the packet undergo their individual life cycles. The envelope is found to propagate to the east more rapidly than the phase speed of the individual disturbances, so that these eddies can be said to undergo "downstream development." Downstream development is often observed in the NH (Namias and Clapp 1944; Hovmöller 1949; Joung and Hitchman 1982), but it is ubiquitous in the SH summer. Van Loon (1965) and Trenberth (1986) show clear examples, and Orlanski and Katzfey (1991) provide a detailed analysis of a particular case.

Models of downstream development have been studied by Simmons and Hoskins (1979) and Orlanski and Chang (1993). In the linear evolution of a localized perturbation to a baroclinically unstable flow, new disturbances develop downstream and depending on the model and the mean flow, also upstream of the original disturbance, and the unstable packet spreads in time. Nonlinearity must be invoked to explain solutions in

* Present affiliation: Advanced Study Program, National Center for Atmospheric Research, Boulder, Colorado.

Corresponding author address: Dr. Sukyoung Lee, Advanced Study Program, NCAR, P.O. Box 3000, Boulder, CO 80307-3000.

which the packet envelope propagates steadily, with a well-defined group velocity, while retaining its shape. The nonlinear Schrödinger equation is the classic example of an equation that possesses just such a solution (e.g., Whitham 1974). In the literature on weakly nonlinear baroclinic instability, coherent wave-packet solutions have been discussed by Pedlosky (1972), Moroz (1981), and Moroz and Brindley (1981, 1984). The latter group of papers was motivated by observations of modulated waves in annulus experiments (Hide et al. 1977; Mason 1975). Although they are a natural starting point, for reasons described in the following we suspect that these weakly nonlinear theories are not adequate for studying the SH packets or those found in the atmospheric models that we have examined.

After describing the wave packets in the SH summer, a series of models are discussed: a multilayer general circulation model with a zonally symmetric lower boundary and, therefore, a zonally symmetric climate; a two-level primitive equation model on the sphere; and a two-layer quasigeostrophic (QG) model on a beta-plane. We thereby isolate the baroclinic wave packets in successively simpler dynamical frameworks. In the latter two models the supercriticality of the flow is varied, and in the QG model the size of the domain is also varied, to explore the dependence of the packets on these parameters.

We also examine the statistical structure of the eddies within the packet, emphasizing the east–west asymmetry in this structure resulting from the fact that the youngest eddies are found on the eastern edge of the packet and the oldest on the western edge. We go a step further to show the very close relation between the evolution *in time* of a disturbance consisting of only a single zonal harmonic, and the evolution *in space* of the eddies within a coherent packet. This relation is also shown to hold for the mean flow modification by the eddies, if we define the "mean" to be an average over the fast-phase variations within the packet.

In the concluding section, we briefly address the limitations of weakly nonlinear theory and speculate on the importance of such packets for atmospheric predictability.

2. Observations

First we describe baroclinic wave packets in observations from the Southern Hemisphere (SH). The data used in this study are derived from the ECMWF analyses at 0000 and 1200 UTC. The dataset covers January 1980 to December 1987.

Snapshots of the eddy (deviation from the zonal mean) meridional wind field, v', at 300 mb are shown in Fig. 1. These fields are taken at 0000 UTC on 3–8 February 1984 (days 1–6 hereafter). At day 1, there are two wave packets in the domain, one centered near

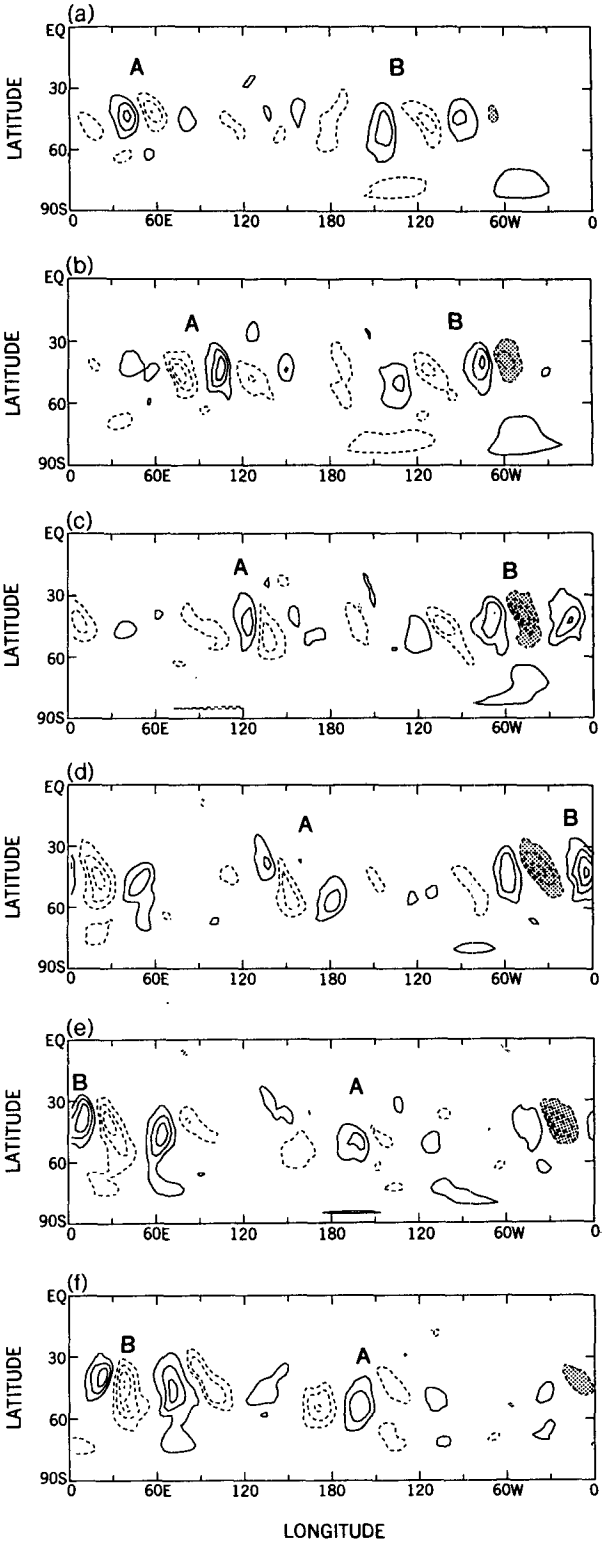

FIG. 1. Snapshots of the eddy meridional wind fields at 300 mb during (a) 3 February–(f) 8 February 1984. The contour interval is 15 m s^{-1}. For clarity, the zero contour is omitted. Solid contours are positive and dashed contours negative.

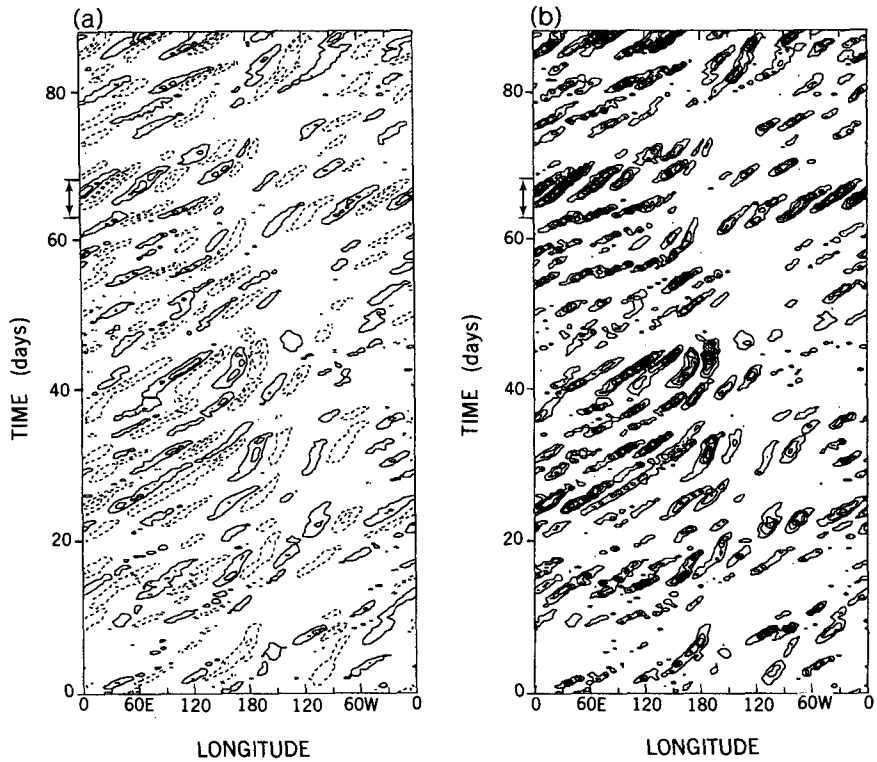

FIG. 2. Hovmöller diagrams of (a) eddy meridional wind and (b) eddy meridional wind squared during DJF of 1983/84 in the SH at 45°S and 300 mb. The contour intervals are (a) 20 m s^{-1} and (b) 400 m^2 s^{-2}. In (a) the zero contour is omitted, solid contours are positive, and dashed contours negative.

45°E (Packet A) and the other near 120°W (Packet B). The packets move toward the east with a speed of about 30 deg day^{-1}. By day 4, Packets A and B have moved near 150°E and the Greenwich meridian, respectively. Packet A appears to lose some of its coherence after day 4, whereas Packet B continues to propagate steadily. Note that the individual eddies decay or grow, while traveling toward the east about 3–4 times slower than the wave packets. For example, a weak minimum (indicated by the shaded area) in the downstream side of Packet B, near 60°W at day 1, intensifies until day 3. By this time, it has moved only 15 degrees toward the east. As this minimum moves toward the upstream side of Packet B, it starts to decay; at day 6, it lies near 10°W and is about to disappear.

The propagation of coherent wave packets, depicted in Fig. 1, is easily illustrated with a longitude–time, or Hovmöller, contour diagram. Figure 2a shows a Hovmöller diagram of the v' field at 45°S and 300 mb during the SH summer (December–February, DJF) in 1983/84. A Hovmöller diagram of v'^2 is also included in Fig. 2b because this sometimes allows the packet to be more easily identified. The period corresponding to Fig. 1 is indicated by the arrows to the left of the figures. Data from other SH summers exhibit similar characteristics to those shown in Fig. 2. The eastward-propagating wave packets often disappear between the date line and 100°W where the mean flow is anticyclonic and climatological eddy energy is weak. Constructing a Hovmöller diagram by following a mean streamline rather than a latitude circle does not alter this picture significantly. Although the stationary wave seems to prevent the wave packet from propagating directly to the east at times, there are a few events where the wave packet propagates through this region and circles the globe, as shown in Fig. 1.

The winter season for the SH midlatitudes has also been examined. Wave packets are found in the winter SH, but seem to be less coherent than in summer. One-point correlation maps in longitude and time (Fraedrich and Ludz 1987) are useful in comparing the seasons. Ignoring the zonal asymmetries in eddy statistics for this purpose, average maps are computed with the base point set equal to each grid point at 45°S to obtain a single correlation map for v'. Figures 3a and 3b are the composites of the maps for summer and winter using seven years of data. They are obtained by computing maps for each season (DJF and JJA) and each year (1980–1987) and then averaging for each season. The correlations are larger in summer than in winter,

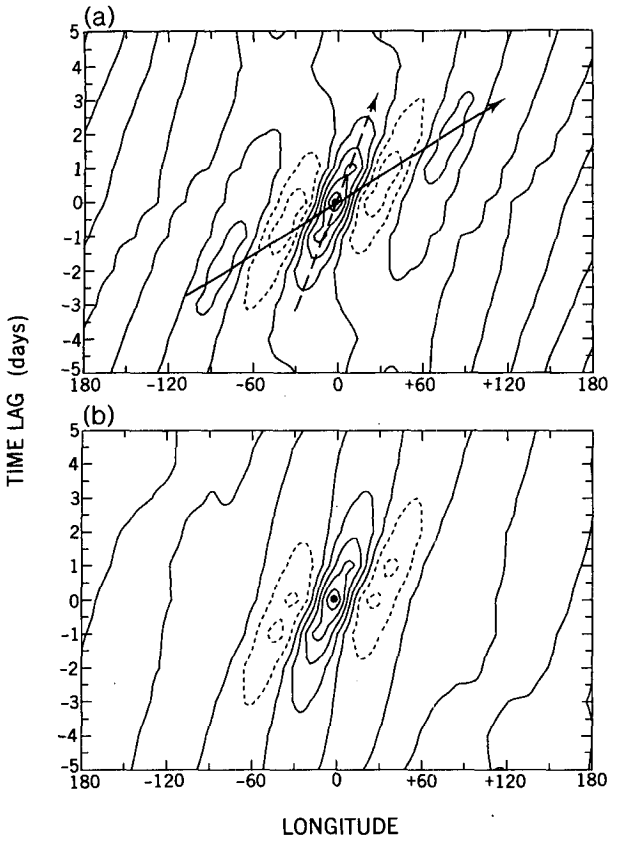

FIG. 3. Composite one-point correlation maps of eddy meridional wind at 45°S and 300 mb in the longitude-time domain for (a) the summer and (b) the winter season during 1980–1987. The contour interval is 0.2, with the dashed contours being negative. The base point is indicated with a filled dot. In (a), solid arrow indicates group velocity, and dashed arrow phase velocity.

consistent with packet being more prominent in summer. The group velocity of the packet and phase speed of the eddies can be estimated as shown in Fig. 3. For both summer and winter seasons, the velocity of the packet is greater than the phase speed of the individual disturbances, implying downstream development. In the summer composite, eddies dominated by zonal wavenumber 6 propagate at about 7 m s^{-1}, whereas the group velocity is about 35 m s^{-1}.

Figures 4a and 4b are longitude–time (ω–k, hereafter) spectra of v' at 45°S and 300 mb averaged over 7 summers and 7 winters. The group velocity $\partial\omega/\partial k$ can be estimated by computing a finite differenced $\Delta\omega/\Delta k$ using the ω–k spectra; in Fig. 4a, the spectral peaks at zonal wavenumbers 6 and 7 are at frequencies of 0.16 and 0.26 $days^{-1}$, respectively. The slope $\Delta\omega/\Delta k$ gives a value of 35 m s^{-1}, consistent with the value obtained from the one-point correlation map.

There are at least three reasons why the SH summer might be expected to possess more coherent wave packets than SH winter: 1) Eddies have somewhat larger scales in winter. As seen in Fig. 4, wavenumbers 4–6 dominate in winter, as compared to 5–7 for summer. One suspects that larger eddies are more difficult to organize into coherent wave packets, due to the weaker scale separation between the envelope and the eddies themselves. 2) Stationary eddies are stronger in winter, making coherent propagation more difficult. 3) The summer storm track is much more confined meridionally (e.g., Randel and Held 1991, Fig. 5). Since coherent eddies are generally easier to obtain when there is only one dimension in which the eddies can propagate, this meridional confinement could favor coherence. [One would also expect more coherent eddies when the flow is less strongly unstable, but the maximum baroclinicity and eddy kinetic energies appear to be comparable in SH winter and summer (Trenberth 1982); the summer time eddies and baroclinicity are weaker only in the sense of being more strongly confined meridionally].

3. An idealized GCM

This model is a 9-level, R30, σ-coordinate, global spectral model developed at GFDL. The details of the model can be found in Manabe et al. (1979) and Gor-

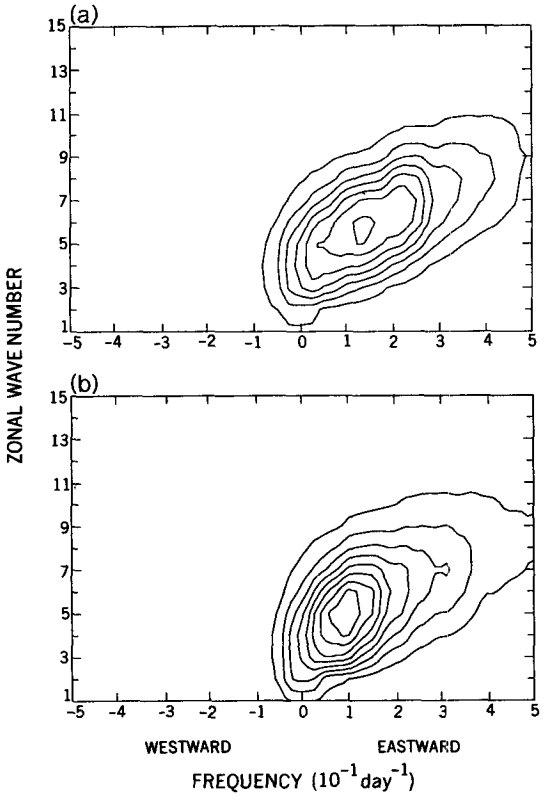

FIG. 4. Composite space-time (ω–k) spectra of eddy meridional wind for (a) the summer and (b) the winter season during 1980–1987. The contour interval is 10 m^2 $s^{-2}/\Delta\omega$.

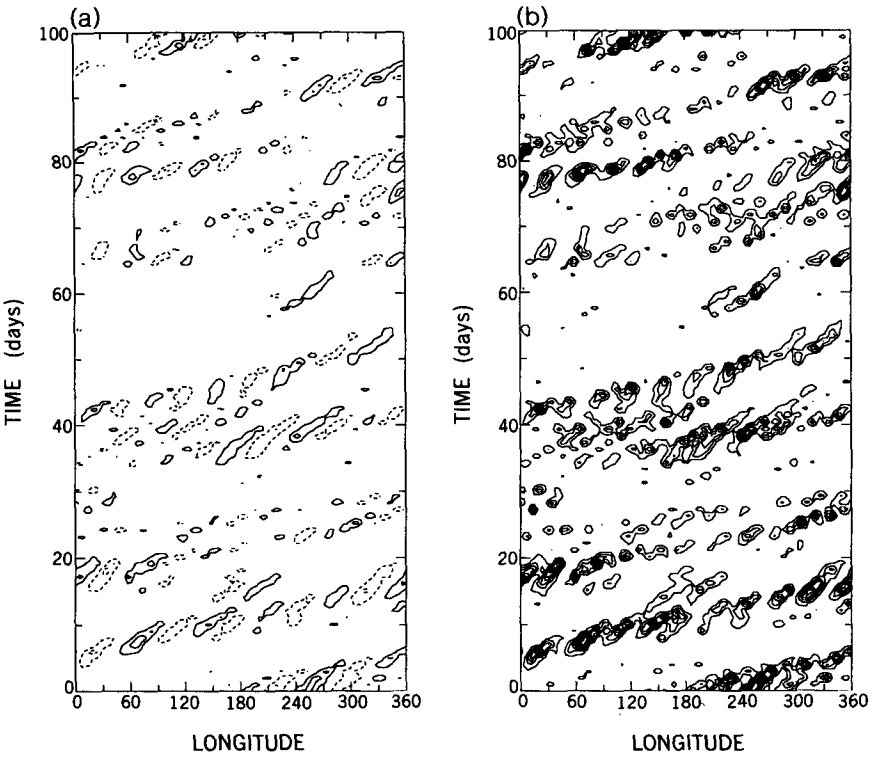

FIG. 5. Hovmöller diagrams of (a) eddy meridional wind and (b) eddy meridional wind squared for 100 days at 35°C and 205 mb in the idealized GCM experiment. The contour intervals are (a) 20 m s^{-1} and (b) 300 m^2 s^{-2}. In (a) the zero contour is omitted, solid contours are positive, and dashed contours negative.

don and Stern (1982). In this version of the model, the lower boundary condition is an all-ocean surface with a zonally symmetric surface temperature distribution of the form

$$T_S = 290\ \text{K} + \frac{40\ \text{K}}{3}(1 - 3\sin^2\phi). \qquad (1)$$

The model contains a full hydrologic cycle, including cloud prediction. Insolation is given its annual mean value. After 2000 days of integration, the model climate is very close to being zonally symmetric. The two hemispheres of the model are also statistically identical.

Figures 5a and 5b show the Hovmöller diagram of v' and v'^2, for 100 days from the 2000-day integration. In this idealized GCM, the midlatitude storm track lies about 10° equatorward of its observed location near 45°. Therefore, the data are sampled at 35° and 205 mb. In Fig. 5, coherent wave packets are very clearly seen. Again, downstream development associated with the packet is evident. The structure of the ω–k spectrum of the GCM data (not shown) is also very similar to that of the SH summer. As might be anticipated due to the horizontally homogeneous lower boundary of the model, the wave packets are somewhat more coherent here than in the SH observations. In fact, between days 1 and 25, in Fig. 5, a coherent packet can be seen propagating twice around the earth. This model allows us to conclude that the packets observed in the SH are not a consequence of some peculiarity of the earth's surface, such as the Antarctic plateau. Further analysis of the GCM data will be presented in section 6.

4. A two-level primitive equation model

a. Model description

The two-level primitive equation model used in this study is essentially identical to that of Hendon and Hartmann (1985). A pressure coordinate, global spectral model with finite differencing in the vertical is used. The spherical harmonic expansion is truncated at R30. The horizontal velocity and potential temperature are predicted at P_1 = 250 mb and P_2 = 750 mb. (The subscripts 1 and 2 refer to the upper and lower levels, respectively.) The "vertical velocity" ω ($=dP/dt$) is defined at 500 mb and at the upper and lower boundaries, where it is set to zero.

We define barotropic and baroclinic variables,

$$\bar{u} = \frac{u_1 + u_2}{2}$$

and

$$\hat{u} = \frac{u_1 - u_2}{2}.$$

The model can be written as four prediction equations for the barotropic and baroclinic vorticity, baroclinic divergence, and barotropic potential temperature:

$$\frac{\partial \bar{\zeta}}{\partial t} = -\nabla\cdot[(f+\bar{\zeta})\bar{\mathbf{u}} + \hat{\zeta}\hat{\mathbf{u}}] - \nabla\times(\hat{D}\hat{\mathbf{u}}) - \frac{\kappa_2}{2}\bar{\zeta} + \frac{\kappa_2}{2}\hat{\zeta} - \nu\left(\frac{2}{a^2}+\nabla^2\right)^4\bar{\zeta}, \quad (2.a)$$

$$\frac{\partial \hat{\zeta}}{\partial t} = -\nabla\cdot[(f+\bar{\zeta})\hat{\mathbf{u}} + \hat{\zeta}\bar{\mathbf{u}}] + \frac{\kappa_2}{2}\bar{\zeta} - \frac{\kappa_2}{2}\hat{\zeta} - \nu\left(\frac{2}{a^2}+\nabla^2\right)^4\hat{\zeta}, \quad (2.b)$$

$$\frac{\partial \hat{D}}{\partial t} = \nabla\times[(f+\bar{\zeta})\hat{\mathbf{u}} + \hat{\zeta}\bar{\mathbf{u}}] - C_pB\nabla^2\bar{\theta} - \nabla^2\hat{E} - \frac{\kappa_2}{2}\hat{D} - \nu\left(\frac{2}{a^2}+\nabla^2\right)^4\hat{D}, \quad (2.c)$$

$$\frac{\partial \bar{\theta}}{\partial t} = \nabla\cdot[\bar{\theta}\bar{\mathbf{u}}] - \hat{\theta}_0\hat{D} - r(\bar{\theta}-\bar{\theta}_e) - \nu\nabla^8\bar{\theta}, \quad (2.d)$$

where $\mathbf{u} = (u, v)$ is the horizontal velocity,

$$\zeta = \nabla\times\mathbf{u}, \quad D = \nabla\cdot\mathbf{u}, \quad \hat{E} = \bar{\mathbf{u}}\cdot\hat{\mathbf{u}},$$

and

$$B = \frac{1}{2}\left[\left(\frac{P_2}{P_s}\right)^\kappa - \left(\frac{P_1}{P_s}\right)^\kappa\right] = 0.124,$$

with $\kappa = 2/7$. The vertically averaged divergence is assumed to vanish identically.

The value of the static stability $\hat{\theta}_0$ is fixed as 15 K. The value of $\bar{\theta}_e$ is

$$\bar{\theta}_e = \frac{\theta_m}{3}(1 - 3\sin^2\phi), \quad (3)$$

where ϕ is latitude and θ_m is the temperature difference between the pole and equator in radiative equilibrium.

Only the lower-level wind is subject to mechanical damping, for which the value of the coefficient κ_2 is 0.2 day^{-1}. The radiative relaxation time scale, r^{-1} is 30 days. The coefficient of the quad-harmonic horizontal diffusion ν is chosen as 8×10^{38} m^8 s^{-1}. Although this value is somewhat larger than it need be, it does not damp the large-scale motion significantly. When the model is integrated with a smaller value of ν ($=8\times10^{37}$), our results are essentially unchanged. The time stepping procedure includes implicit treatment of the terms responsible for gravity waves.

b. Results

The value of θ_m [in (3)] is systematically varied in order to study the effect of supercriticality on the wave packets. Figures 6a–c show Hovmöller diagrams of the variance of the upper-level meridional wind $v_1'^2$, at a latitude slightly poleward of the jet maximum for 100 days of 1000-day integrations for θ_m = 80 K, 60 K, and 30 K. The peaks in the spectrum of $v_1'^2$ are centered at zonal wavenumbers 4, 5, and 7 for θ_m = 80 K, 60 K, and 30 K, respectively. Figure 6 shows that wave packets become more coherent as the supercriticality is decreased. When θ_m = 80 K, propagating packets form occasionally (Fig. 6a). When θ_m is decreased to 60 K, wave packets occur more frequently (Fig. 6b). When θ_m is further decreased to 30 K, well-defined packets emerge and remain coherent for a very long time (Fig. 6c). Note also that in the 30 K case there are two distinct wave packets in the domain. Time-lagged one-point correlation maps using time series of 1000 days are shown in Figs. 7a–c. It is clear that the signal of the wave packets becomes stronger as θ_m decreases. Also, the velocity of the packet is always larger than the phase velocity of the individual waves, typically by a factor of 3.

In each case, the group velocity estimated from the slope of the ω–k spectrum and that obtained from the correlation maps agrees very well. The group velocity is always close to the speed of the upper-level zonal wind.

5. A two-layer quasigeostrophic model

a. Model description

The dimensionless equations of our quasigeostrophic (QG) two-layer model on a beta-plane are

$$\frac{\partial Q_1}{\partial t} + J(\Psi_1, Q_1) = r\left(\frac{\Psi_1-\Psi_2}{2} - \tau_e\right) - \nu\nabla^6\Psi_1, \quad (4.a)$$

$$\frac{\partial Q_2}{\partial t} + J(\Psi_2, Q_2) = -r\left(\frac{\Psi_1-\Psi_2}{2} - \tau_e\right) - \kappa_M\nabla^2\Psi_2 - \nu\nabla^6\Psi_2, \quad (4.b)$$

where

$$Q_j = \beta y + \nabla^2\Psi_j + (-1)^j\left(\frac{\Psi_1-\Psi_2}{2}\right), \quad j = 1, 2, \quad (5)$$

and j = 1 and 2 refer to the upper and lower layers, once again. The velocity field is determined by the re-

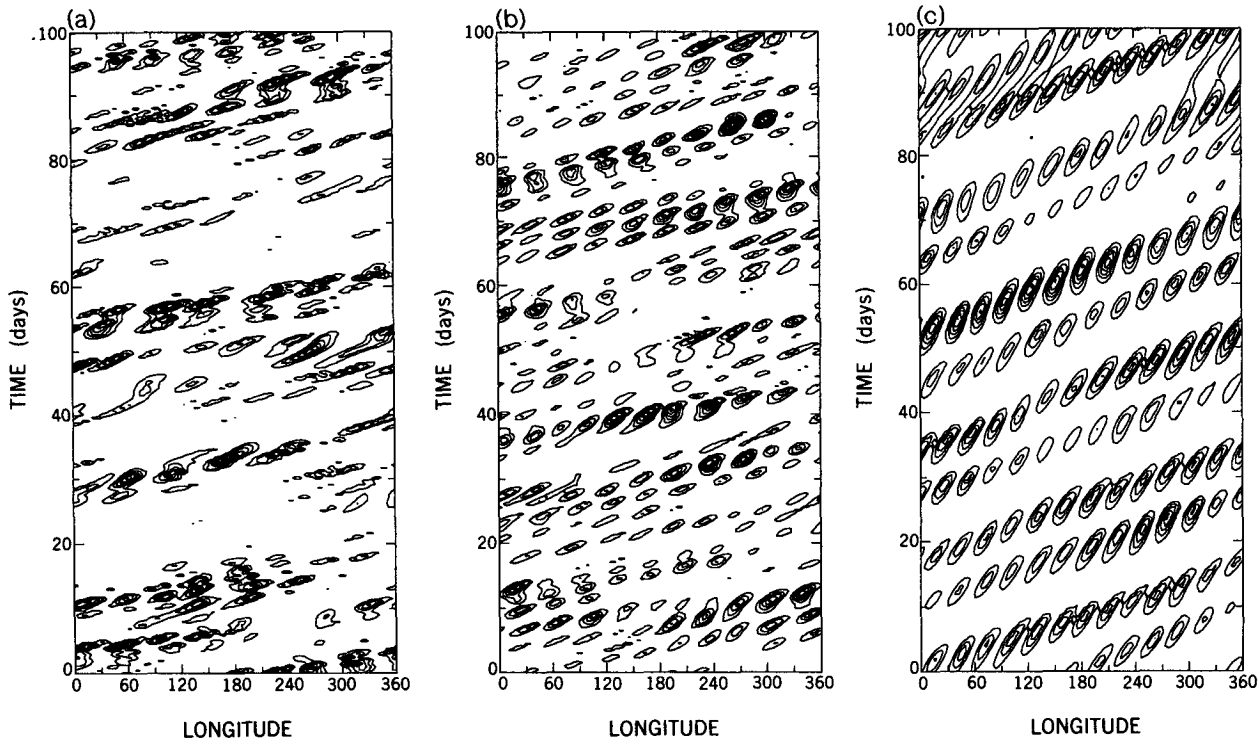

FIG. 6. Hovmöller diagrams of the upper-level eddy meridional wind squared for θ_m = (a) 80 K, (b) 60 K, and (c) 30 K near the midlatitude jet maximum in the two-level PE model. The contour intervals are (a) 700 $m^2 s^{-2}$, (b) 300 $m^2 s^{-2}$, and (c) 100 $m^2 s^{-2}$.

lation, $(u_j, v_j) = (-\partial\psi_j/\partial y, \partial\psi_j/\partial x)$. The horizontal length scale is the radius of deformation, λ. The parameters that remain are κ_M (strength of lower layer drag), r (strength of radiative damping), ν (biharmonic diffusivity), and β (gradient of Coriolis parameter). One can think of β as playing the same role as θ_m in the PE model of section 4, except that the supercriticality of the flow increases as β decreases. Time is nondimensionalized by λ/U_0, where U_0 is the horizontal velocity scale.

A Gaussian zonal wind shear of the form

$$U_e = -2\partial\tau_e/\partial y = \exp[-(y - W/2)^2/\sigma^2]$$

balances the "radiative equilibrium temperature," $\tau_e(y)$, with $\sigma^2 = 10$. The channel walls are located at $y = 0$ and W (=21). This channel width is sufficient that the eddies are confined away from the walls, so the precise value of W should be irrelevant. A thermal relaxation time scale ($=r^{-1}$) is held fixed at 30 days (1 "day" = λ/U_0). The model is finite differenced in the meridional direction and is spectral in the zonal direction. Since this model is identical with that in Lee and Held (1991, LH hereafter), the reader is referred to that paper and references therein for further description.

We found it convenient to utilize three different resolutions in different parts of this study. The grid points between the channel walls, number of zonal waves, and biharmonic diffusion coefficients for those three models are listed below:

	High	Medium	Low
Grid points	600	300	70
Number of the zonal waves	40	20	20
Biharmonic diffusion coefficient	3×10^{-5}	7×10^{-4}	6×10^{-3}

b. Results

The discussion of this model is made more complex by the existence of hysteresis and subcritical instability, as described in LH. Typically, as one increases β, the eddy energy in the statistically steady state does not decrease to zero smoothly as the linear stability boundary, β_0, is approached. Instead, nonzero eddy amplitudes are found up to $\beta_H > \beta_0$, beyond which the eddy amplitude collapses to zero. Since the flow with no eddies present is stable for $\beta > \beta_0$, two distinct solutions exist for β between β_0 and β_H: one with zero eddy amplitude and one with nonzero eddy amplitude. In fact, the region with two distinct stable solutions generally extends to the smaller value $\beta_L < \beta_0$. In the range $\beta_L < \beta < \beta_0$, two distinct states with nonzero eddy

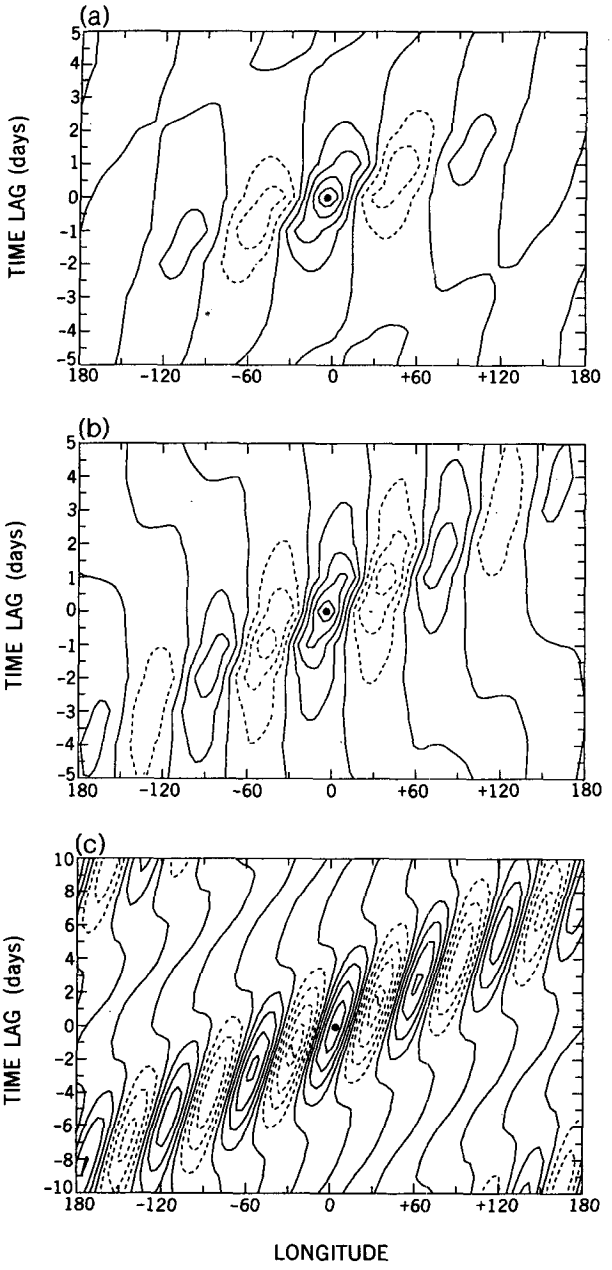

FIG. 7. One-point correlation maps of the upper-level eddy meridional wind in the longitude–time domain for θ_m = (a) 80 K, (b) 60 K, and (c) 30 K near the midlatitude jet maximum in the two-level PE model. The contour interval is 0.2. The base point is indicated by a filled dot.

amplitudes exist, which we refer to as the "upper" and "lower" branches. (The difference between β_L and β_0 is particularly sensitive to resolution and the strength of the diffusivity in the model.) As κ_M is reduced, β_L approaches β_H, until the multiple solutions disappear at a critical value of κ_M ($\approx$0.05). Coherent packets are found in a large part of this model's parameter space—in the linearly unstable region as well as in the linearly stable region. They can also be found both in the upper and lower branches when these exist at the same parameter setting.

This model is first used to examine the transition from a zonally symmetric baroclinic wave train to a localized wave packet. For this purpose, we use the low-resolution model with $\kappa_M = 0.05$, and vary β to change the supercriticality. This value of κ_M is small enough that we find a unique statistically steady state for each value of β (in the low-resolution model). The linear stability boundary, β_0, is 0.38. The eddy amplitudes are steady for $0.3 < \beta < 0.38$ and periodic for $0.23 < \beta < 0.3$. In a higher resolution, less diffusive version of the model these states all become chaotic. We have chosen the low-resolution more diffusive model here in the hope that these nonchaotic flows would be easier to analyze.

Linear growth rates as a function of zonal wavenumber are displayed in Table 1 for several values of β. The 20 zonal wavenumbers retained in the model range from $k = 0.1$ to 2.0 in steps of 0.1 [so the length of the channel, L, is $2\pi/(0.1) = 20\pi$, in units of λ]. For $\beta \geq 0.33$, only one of these waves ($k = 0.8$) is unstable. When β falls below 0.32, the growth rates for 0.7 and 0.9 become significant.

A steady periodic wave train is produced by this model for $\beta > 0.32$, in the cases when only one retained wavenumber has nonnegligible growth rate. Figure 8 displays instantaneous pictures of upper-layer eddy streamfunction for β = 0.31, 0.30, 0.27, 0.24, 0.22, and 0.20. For $\beta = 0.31$, a broad packet has emerged, which propagates steadily with constant amplitude. For $\beta = 0.3$, the width of the packet decreases, but the amplitude remains steady. For $\beta = 0.27$ and 0.24, the width and amplitude of the packet oscillate periodically. In Figs. 8c and 8d the flow is shown at a time at which the width of the packet is a minimum; the maximum width of the packet is similar to that in Fig. 8b. As β is reduced further, the packet splits into two: when $\beta = 0.22$ (Fig. 8e), there is a hint of separation, while two distinct wave packets form for $\beta = 0.20$. The solution for $\beta = 0.20$ is chaotic in time.

To examine the time dependence of the amplitude and width of the packets more systematically, these quantities need to be defined objectively. The envelope of the packet is defined by "demodulating" the spatial structure of the streamfunction (in the upper layer, at the center of the channel) at each instant of time. Demodulation is an algorithm that separates the modulating envelope from the carrier wave (e.g., see Bloomfield 1976). It requires the specification of the carrier wavelength, but our results are not sensitive to its precise value. The maximum amplitude of the packet, A, is set equal to the maximum value of the envelope function. The width of the packet, W, is then calculated

TABLE 1. Linear growth rates, ω_i ($\times 10^{-2}$), of the most unstable mode for $\kappa_M = 0.05$ in the low-resolution model.

	k									
β	0.675	0.700	0.725	0.750	0.775	0.800	0.825	0.850	0.875	0.900
0.30	0.65	1.56	2.28	2.79	3.07	3.13	2.98	2.59	1.95	1.02
0.31	0.13	1.05	1.80	2.34	2.66	2.76	2.64	2.27	1.65	0.73
0.32		0.53	1.31	1.89	2.25	2.38	2.28	1.94	1.34	0.42
0.33		0.03	0.82	1.43	1.82	1.99	1.92	1.60	1.01	0.09
0.34			0.32	0.96	1.39	1.58	1.54	1.25	0.67	
0.35				0.49	0.94	1.17	1.16	0.88	0.32	
0.36				0.01	0.49	0.74	0.76	0.51		
0.37					0.03	0.31	0.35	0.12		

by identifying the two locations where the amplitude of the envelope is half of A.

Figs. 9a–c show A as a function of W for $\beta = 0.28$, 0.24, and 0.23, with the same value of κ_M (0.05). Both A and W are essentially periodic in time, the small scatter in the figures resulting from the demodulating algorithm. For $\beta = 0.28$, there is a clear negative correlation between A and W. However, W takes on different values depending on whether A is increasing or decreasing, resulting in a loop in A–W space. When $\beta = 0.24$, this loop opens up further. When β is reduced to 0.23, the loop is broken as A increases (near $A = 2.7$), signaling the start of the breakup of the single packet.

The nonlinear Schrödinger equation (NLS hereafter) has been used to describe coherent wave packets in many different fields, ranging from solid state physics to fluid mechanics (Whitham 1974). A coherent, steadily propagating wave packet is one of the exact solutions of the NLS equation. This solution states that the amplitude and width of the packet are inversely proportional to each other, while both the amplitude and width are independent of the velocity of the packet, the latter being equal to the group velocity determined by the underlying linear dispersion relation.

The negative temporal correlation between A and W in Fig. 9 suggests that the NLS equation may mimic some of the dynamical balances maintaining the pack-

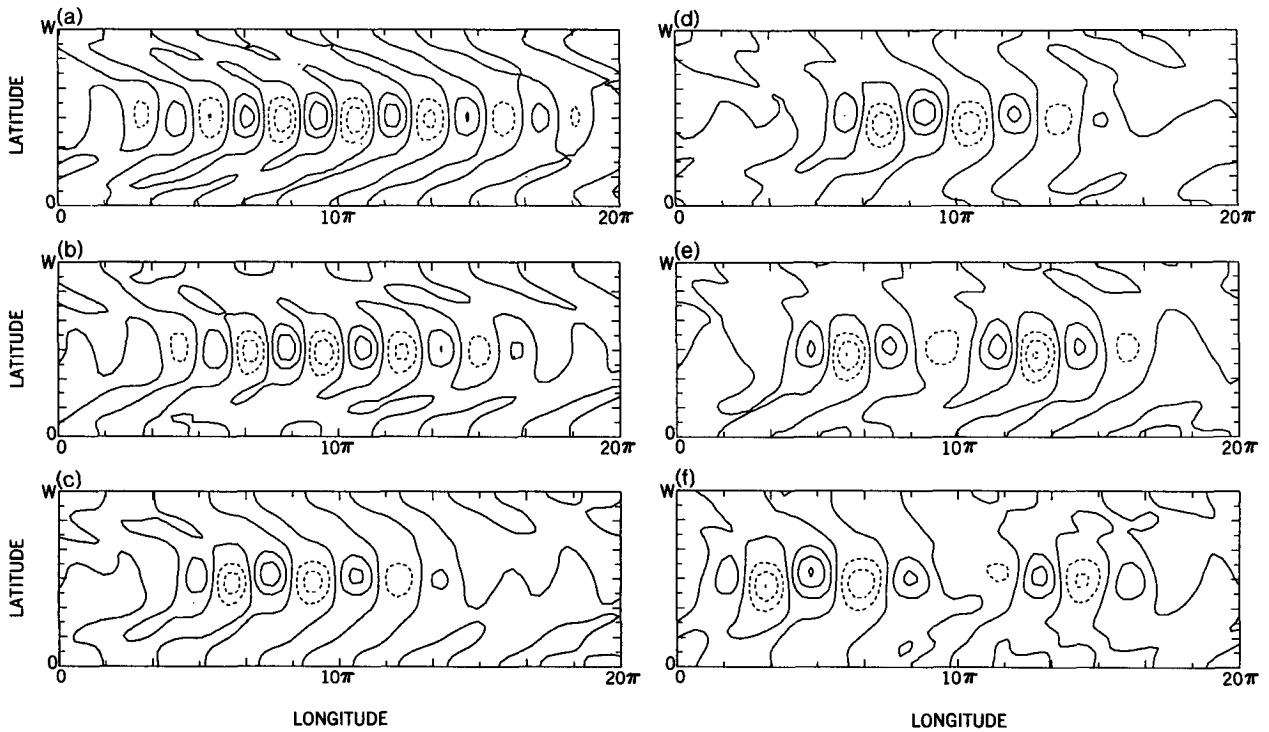

FIG. 8. Snapshots of upper-layer eddy streamfunction from the low-resolution QG model for β = (a) 0.31, (b) 0.30, (c) 0.27, (d) 0.24, (e) 0.22, and (f) 0.2, with $\kappa_M = 0.05$. Contour intervals are (a) 0.4, (b) 0.5, (c) 0.8, (d) 1.0, (e) 1.0, and (f) 1.0.

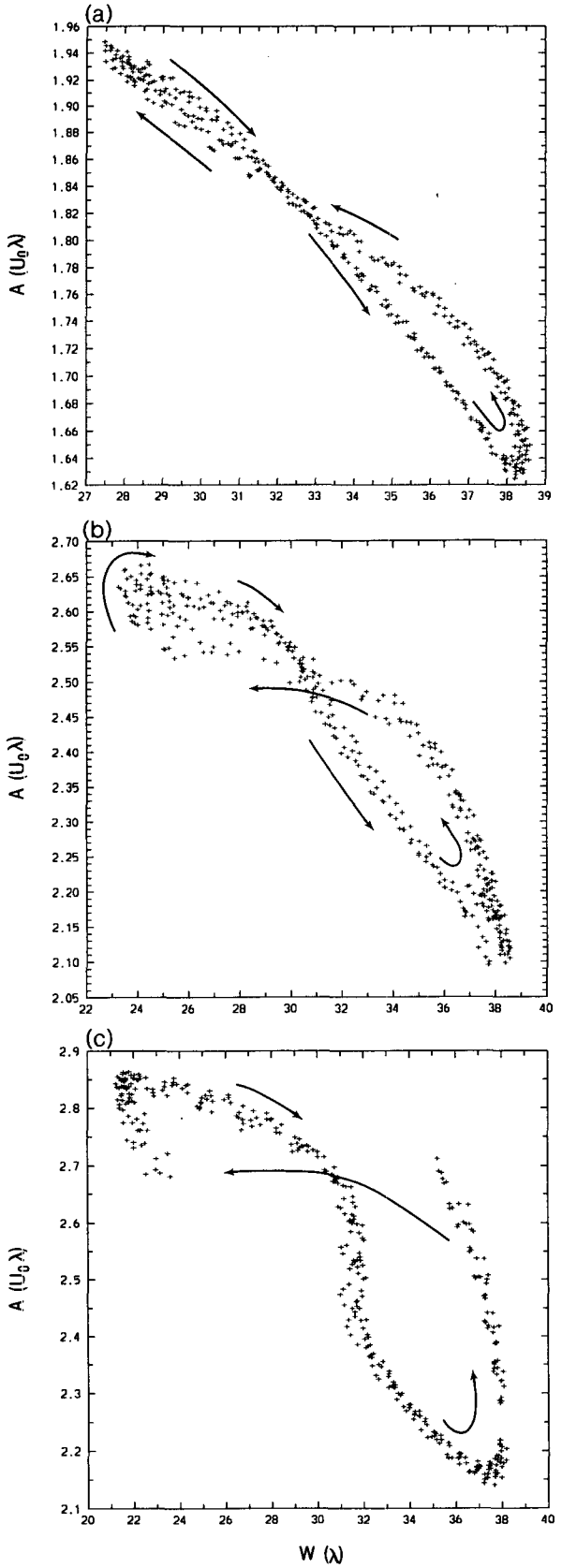

ets. We have also estimated the speed of the packets and find no correlation between this speed and either A or W.

Instead of increasing the supercriticality, one can also obtain multiple wave packets by increasing the channel length. We choose the $\beta = 0.30$ case (see Fig. 8b) of the low-resolution model as a control run. When the channel length is doubled (by halving the fundamental wavenumber and doubling the number of waves, so that the length of the channel L is 40π, maintaining the same zonal resolution), two wave packets emerge. When the channel length is quadrupled ($L = 80\pi$), five packets emerge. Figures 10a and 10b display snapshots of the upper-layer streamfunction from the low-resolution model in these unrealistically long channels. These packets propagate without changing their shape and amplitude. For $L = 40\pi$ (see Fig. 10a) both the width of the packet and the wavenumber of the carrier waves ($k = 0.8$) are essentially identical to those for $L = 20\pi$ (see Fig. 8b). The spectrum of the upper-layer eddy streamfunction for $L = 40\pi$, shown in Fig. 11a, indicates that there are two dominant zonal wavenumbers, 0.8 and 0.7.

For $L = 80\pi$, the width of packet seems to be slightly narrower than for $L = 20\pi$ and 40π. Figure 11b shows the zonal wavenumber spectrum of the eddy streamfunction for the $L = 80\pi$ case. The dominant zonal wavenumbers are 0.7 and 0.825. The latter is not resolved for the shorter channels, but it is close to $k = 0.8$, giving packets whose size is comparable with that in the shorter channels. Note that the zonal wavenumbers between 0.725 to 0.8 have negligible energy. In order to examine whether this behavior depends on the initial conditions, we have integrated the model with the amplitude of the initial disturbances with zonal wavenumbers from 0.725 to 0.8, an order of magnitude larger than that of the other zonal wavenumbers. The energy of these zonal wavenumbers was found to decay to zero after a long transient stage.

The packet structure has also been examined in a few selected integrations with the medium-resolution model, once again with $\kappa_M = 0.05$. For the standard channel length of 20π, one packet emerges for $\beta = 0.34$ and 0.30, and remains very coherent, even though the amplitude and width of the packet evolve in a much more chaotic manner than in the low-resolution model. Plots similar to those in Fig. 9 show no clear patterns, although there still could be relationships between A and W discoverable by other means. (For $\beta = 0.34$, two branches of solutions exist in this medium-resolution model, as $\beta_H = 0.346$; we refer here to the upper

FIG. 9. The maximum amplitude, A, as a function of the half-width, W, of the demodulated wave packet in the low-resolution QG model for β = (a) 0.28, (b) 0.24, and (c) 0.23, with $\kappa_M = 0.05$. The "path" of the loop is indicated by arrows.

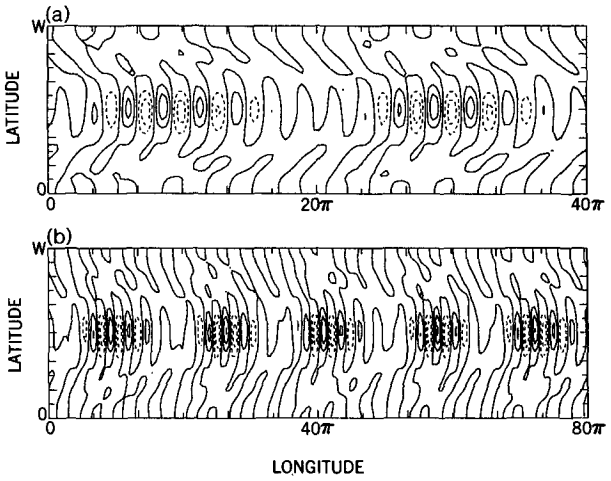

FIG. 10. Snapshots of upper-layer eddy streamfunction from the low-resolution QG model for $\beta = 0.3$ and $\kappa_M = 0.05$, with channel length of (a) 40π and (b) 80π. Contour interval is 0.5.

branch.) The splitting appears to take place near $\beta = 0.25$, at a larger value of β than in the low-resolution model.

This medium-resolution model has also been integrated with a channel length of 40π, setting $\beta = 0.30$. While there is only one packet for $L = 20\pi$, there are three for $L = 40\pi$. The energy spectrum still has two peaks, but they are not as sharp as in the lower-resolution model. The packets at this point of parameter space are not sensitive to the zonal quantization, but there are other points, particularly within the lower branch of solution, near the linear stability boundary, where there does appear to be some sensitivity.

6. The internal structure of the packet

These baroclinic wave packets have an intriguing internal structure that is related to the interaction between the packet and the "mean" flow. The "mean" is defined here as an average over the fast phase variations. Figure 12 shows snapshots of the potential vorticity in both layers together with the upper-layer eddy streamfunction for $\beta = 0.3$ and $\kappa_M = 0.05$. These results are from the high-resolution model. The medium-resolution results are similar but less well defined. The eddy streamfunction (Fig. 12c) shows that the packet is located at the center of the domain. The corresponding Hovmöller diagram (Fig. 13) of the eddy streamfunction at the central latitude clearly shows that the wave packet remains coherent for long times. The upper-layer potential vorticity field (Fig. 12a), however, shows that wave breaking is occurring and mainly on the upstream side of the packet. In the lower layer, potential vorticity mixing occurs at the center of the jet with more vigorous mixing occurring near the upstream side of the packet once again. New waves are developing on the eastern side of the packet; on the western side, wave breaking is dominant. This structure of the baroclinic waves within the packet closely resembles that seen in various stages in the life cycles of baroclinic waves (Randel and Stanford 1985; Simmons and Hoskins 1978; Feldstein and Held 1989). Similar structure is seen at other parameter settings.

The resemblance between the spatial structure of the eddies in the packet and the life cycles of baroclinic waves as a function of time suggests that the maintenance of the wave packet might be related to the mechanism that controls *modal* baroclinic wave life cycles.

We compare the packet structure with the *time* evolution of the eddy statistics and mean flow during *modal* development. For this purpose, we consider a model with a *single zonal wavenumber*. A medium resolution model is utilized, since its solutions are qualitatively similar to those of the high-resolution model, yet it is more efficient to integrate. We choose $\beta = 0.24$ and $\kappa_M = 0.2$. At this parameter setting, the flow is weakly unstable and both lower- and upper-branch solution exist. We focus on the lower branch here, since it produces a simpler life cycle in the one-wave model. We chose $k = 0.72$ once again because the life cycles of the unstable baroclinic waves for this value of k are relatively simple. The flow is very weakly unstable and

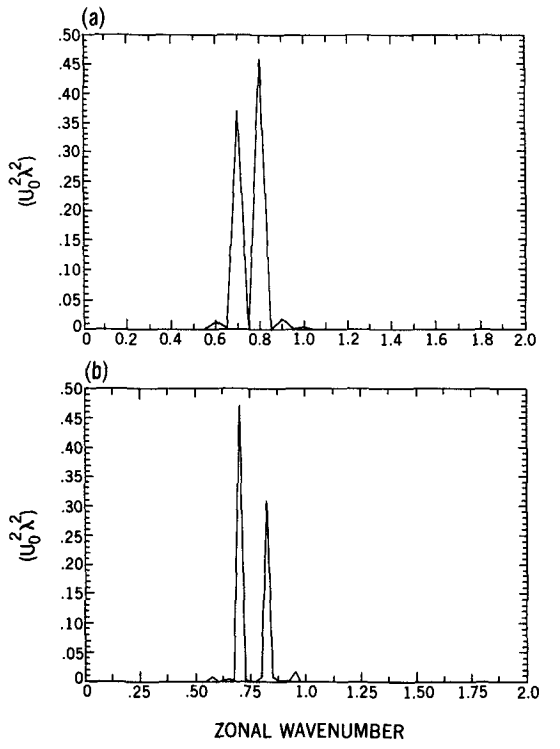

FIG. 11. The upper-layer eddy streamfunction squared as a function of zonal wavenumber from the low-resolution QG model for $\beta = 0.3$ and $\kappa_M = 0.05$ with channel length of (a) 40π and (b) 80π.

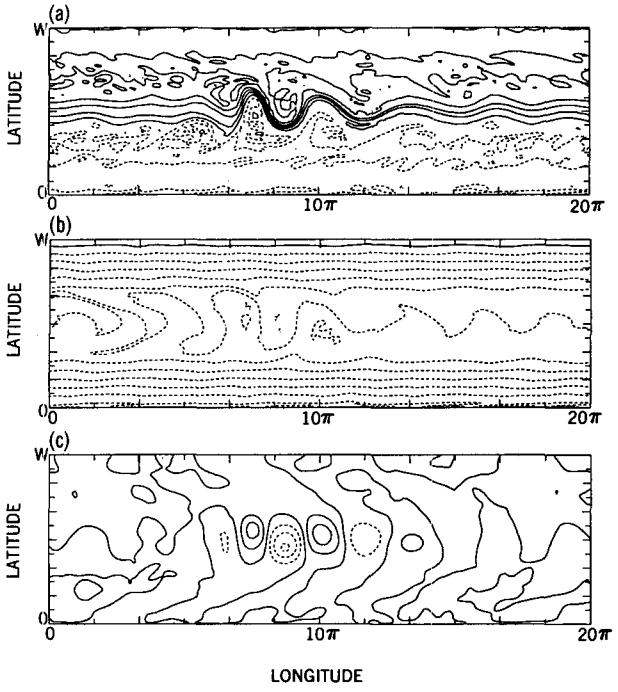

FIG. 12. Snapshots (at $t = 87$ shown in Fig. 13) of potential vorticity for (a) upper layer, (b) lower layer, and (c) the upper-layer eddy streamfunction in the high resolution QG model with $\beta = 0.3$ and $\kappa_M = 0.05$. Contour intervals are (a) 1.0, (b) 0.3, and (c) 1.0.

eddy amplitudes are very small at this parameter setting.

Figures 14a and 14b show the evolution of the zonally averaged eddy streamfunction variances $\overline{\psi_1'^2}$ and $\overline{\psi_2'^2}$ as a function of time for this one-wave model. While the wave grows, the structure of the wave in both layers deviates a little from its linear normal mode structure. During the decay stage, however, the upper-layer streamfunction changes its structure significantly, and the wave amplitudes near the sides of the jet increase. The evolution of $\partial\bar{u}_1/\partial t$ and $\partial\bar{u}_2/\partial t$ is illustrated in Figs. 14c and 14d, respectively; $\partial\bar{u}_2/\partial t$ is largest at the center of the jet, while $\partial\bar{u}_1/\partial t$ is largest at the jet margins, near the linear critical latitudes.

The zonal mean flow in this model evolves according to the equation:

$$\frac{\partial \bar{u}_i}{\partial t} = \overline{v_i' q_i'} + \overline{v_i^T} - \delta_{i,2}\kappa_M \bar{u}_2, \quad i = 1, 2 \qquad (7.a)$$

and

$$\frac{\partial}{\partial t}\left(\frac{\bar{u}_1 - \bar{u}_2}{2}\right) = \frac{\partial^2 \overline{v_1^T}}{\partial y^2} - r\left\{\left(\frac{\bar{u}_1 - \bar{u}_2}{2}\right) - \frac{u_e}{2}\right\}. \qquad (7.b)$$

Here, the overbar refers to the zonal mean, the prime to the deviation from the zonal mean, and $\overline{v_i^T}$ ($\overline{v_1^T} = -\overline{v_2^T}$) is the "residual" circulation (Edmon et al. 1980). An equation for $\overline{v_i^T}$ can be obtained from (7) by eliminating the time tendencies. The small direct effect of diffusion on the mean flow has been neglected in (7). The evolution of the zonally averaged potential vorticity fluxes in both layers is shown in Figs. 14e and 14f, respectively. The structure of $\overline{v_1' q_1'}$ corresponds well to the decelerating region of $\bar{u}_1$ at the sides of the jet (compare Figs. 14c and 14e). Near the end of the life cycles, we find that both the thermal forcing and surface friction are essential in restoring the vertical shear as the disturbance decays, allowing the next disturbance to grow.

This life cycle for a single zonal harmonic is now compared with the structure of waves within a coherent packet, using the medium-resolution multiwave model with 20 zonal wavenumbers (from 0.1 to 2.0). The model parameters are identical with those in the one-wave model discussed above. Once again, we find a remarkably coherent wave packet for this parameter setting.

In order to determine the location of the packet, we perform the following procedure. For each model day, the streamfunction is demodulated so that the location where the maximum amplitude of the packet occurs can be identified. Once this location is known, the coordinate system is translated in such a way that the maximum amplitude of the packet appears at the middle of the domain. In the above process, it is assumed that the wavenumber of the carrier wave is the same as the dominant zonal wavenumber of the streamfunction. Once the packet has been located, we can fast phase average by averaging in time in this moving reference frame.

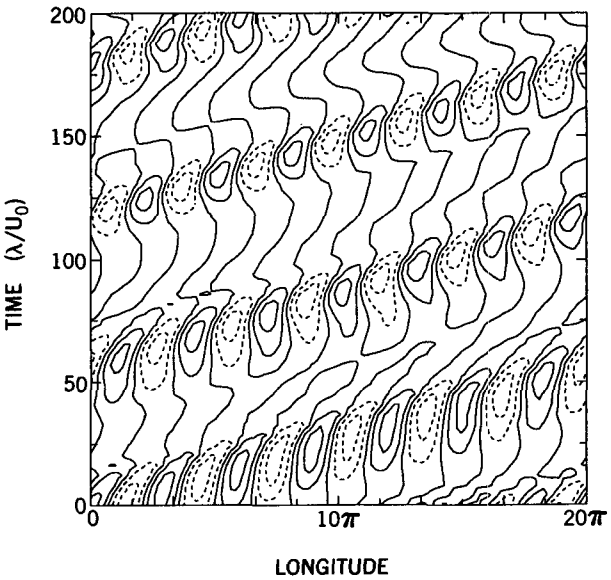

FIG. 13. A Hovmöller diagram of the upper-layer eddy streamfunction at the center of the channel in the high-resolution QG model for $\beta = 0.3$ and $\kappa_M = 0.05$. Contour interval is 1.0.

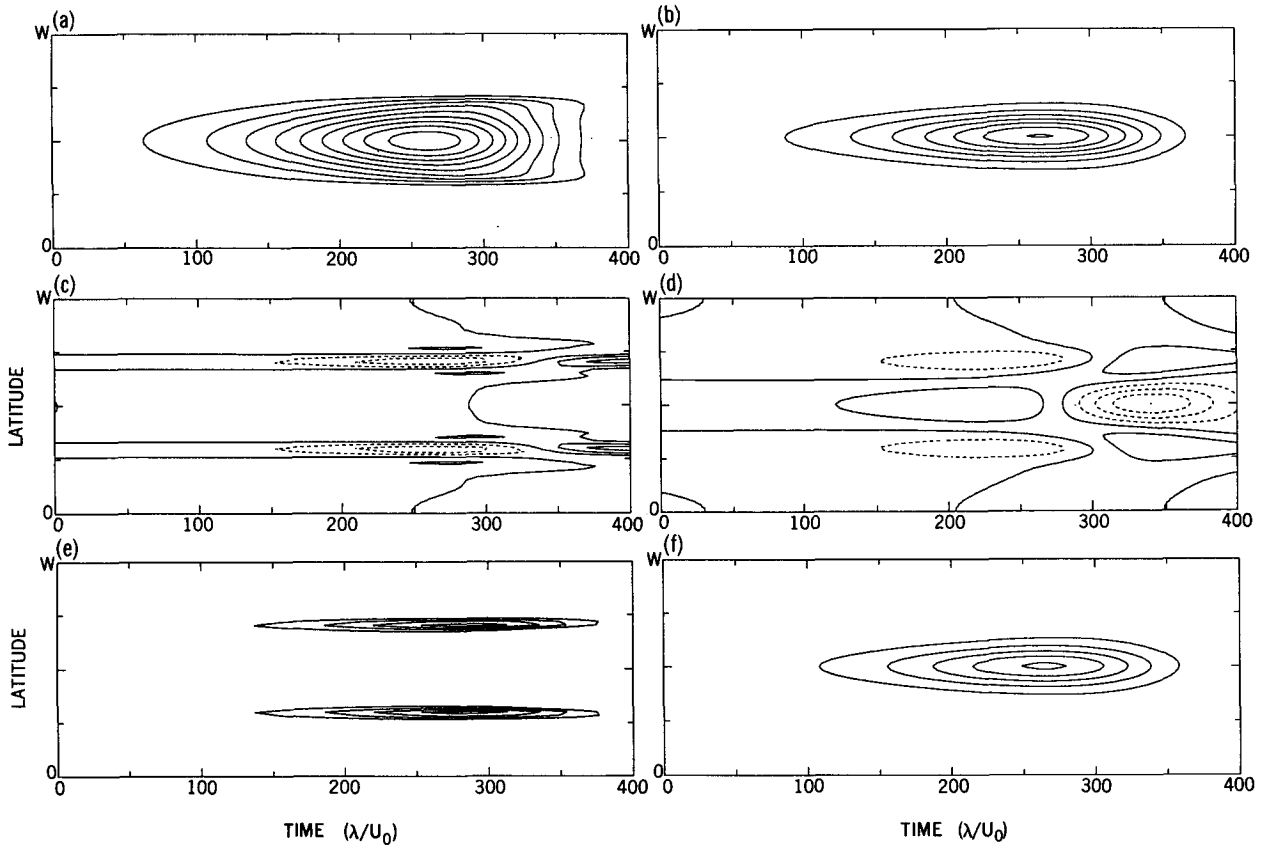

FIG. 14. Latitude–time contours of (a) $\overline{\psi_1'^2}$, (b) $\overline{\psi_2'^2}$, (c) $\partial\bar{u}_1/\partial t$, (d) $\partial\bar{u}_2/\partial t$, (e) $v_1'q_1'$, and (f) $v_2'q_2'$ in the medium-resolution, one-wave QG model with $\beta = 0.24$ and $\kappa_M = 0.2$. Contour intervals are (a) 10^{-4}, (b) 2×10^{-5}, (c) 3×10^{-5}, (d) 2×10^{-6}, (e) 6×10^{-5}, and (f) 3×10^{-5}. In (c), (d), and (f) solid contours are positive, and dashed contours negative. In (e) solid contours are negative, and the zero contour is omitted.

Figures 15a and 15b show the eddy streamfunction amplitude in the upper and lower layers, $\{\psi_1^2(X)\}$ and $\{\psi_2^2(X)\}$, respectively. The brackets refer to averages over the fast phase variations. In the upper layer, one clearly sees the asymmetry of the structure of the streamfunction between the upstream and downstream fringe of the packet. There is a remarkable similarity between the temporal evolution of $\overline{\psi_i'^2}$ (in Figs. 15a and 15b) and the spatial structure of $\{\psi_i^2(X)\}$: the "older" waves are found at the western edge of the packet, because the group velocity is greater than the phase velocity. In both cases, the structure of the streamfunction in the upper layer changes as the wave decays, but in the lower layer the streamfunction structure is essentially unchanged. The *evolution of a wave with increasing time* in the one-wave model is qualitatively similar to that with *decreasing X in the packet.*

In Figs. 15c and 15d, the spatial structure of $-\{\partial u_1/\partial X\}$ and $-\{\partial u_2/\partial X\}$ are shown, respectively. The qualitative structures closely resemble their counterparts $\partial\overline{u_i}(t)/\partial t$ in the life cycle. The structure of $-\{\partial u_i/\partial X\}$ in both layers is slightly asymmetric about the center of the jet. This is because the averaging over phase is not perfect. The eddy zonal wind is antisymmetric about the jet center; if the scale of the eddy is not sufficiently small, the fast phase average is unable to completely remove this asymmetric structure.

The fast phase-averaged eddy potential vorticity fluxes in both layers are shown in Figs. 15e and 15f. Once again, the structure of $\{v_1^* q_1^*\}$ corresponds to the region of negative $-\{\partial u_1/\partial X\}$ at the sides of the jet. In the lower layer, the positive $-\{\partial u_2/\partial X\}$ at the center of the channel is due to forcing by $\{v_2^* q_2^*\}$. The structure of $\{v_i^* q_i^*\}$ in each layer closely resembles the evolution of its temporal counterpart (see Figs. 14e and 14f).

These results encourage us to replace $\partial\overline{u_i}(t)/\partial t$ in (7) with $-C_g\{\partial u_i/\partial X\}$ in a frame of reference moving with the packet, continuing to ignore all x derivatives of eddy statistics. Consistently $\{v^T\}$ at each longitude is computed just as in the zonally symmetric case. The resulting balance is fairly close but not perfect due to the assumption of the scale of the packet being much larger than the scale of the eddies.

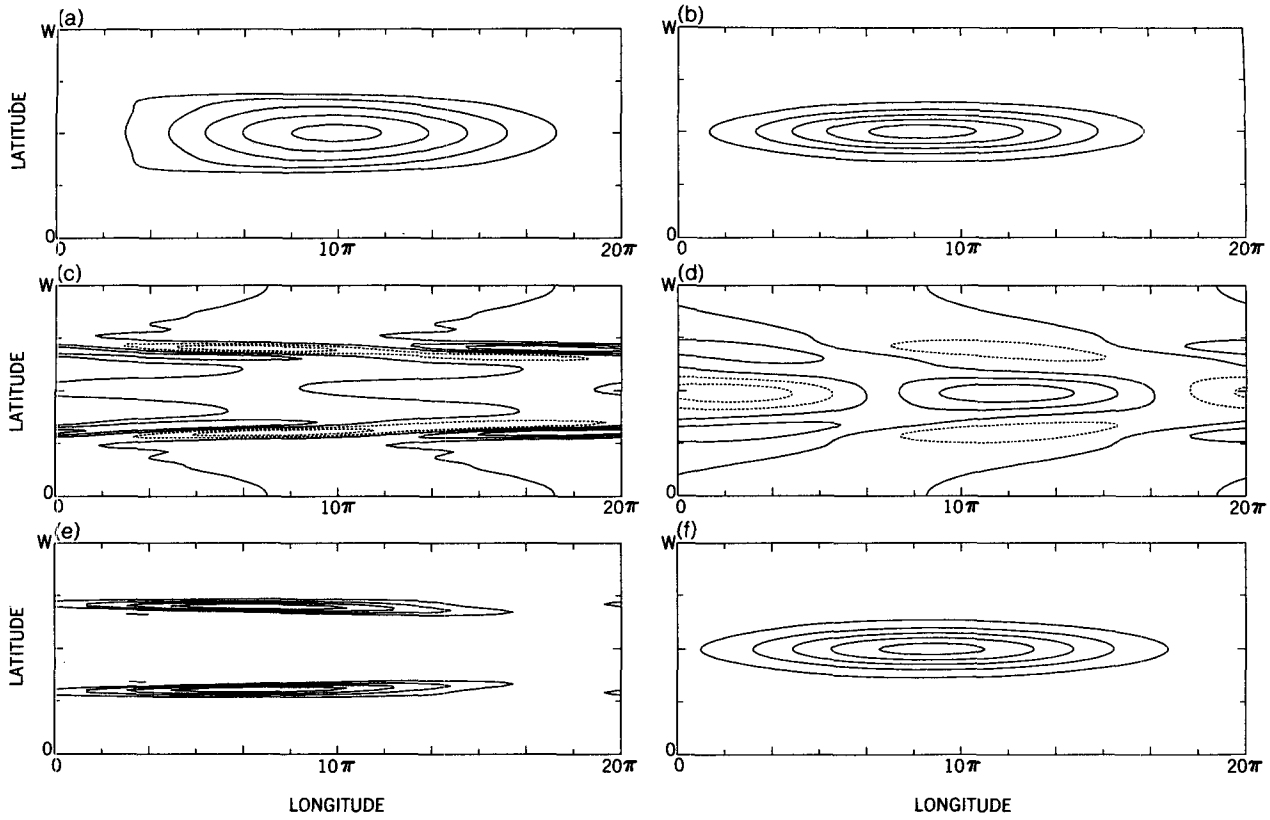

FIG. 15. Latitude–longitude contours of (a) $\{\psi_1^2(X)\}$, (b) $\{\psi_2^2(X)\}$, (c) $-\{\partial u_1/\partial X\}$, (d) $-\{\partial u_2/\partial X\}$, (e) $\{v_1^* q_1^*\}$, and (f) $\{v_2^* q_2^*\}$ in the medium-resolution, multiwave QG model with $\beta = 0.24$ and $\kappa_M = 0.2$. Contour intervals are (a) 2×10^{-4}, (b) 3×10^{-5}, (c) 4×10^{-5}, (d) 6×10^{-6}, (e) 5×10^{-5}, and (f) 3×10^{-5}. In (c), (d), and (f) solid contours are positive, and dashed contours negative. In (e) solid contours are negative, and the zero contour is omitted.

We find that 1) at the center of the jet $\{u_2\}$ increases toward the west (i.e., upstream) due to forcing by $\{v_2^* q_2^*\}$ and 2) at the sides of the jet $\{u_1\}$ decreases toward the west because of $\{v_1^* q_1^*\}$ and, secondarily, the dissipation, whereas $\{u_2\}$ decreases toward the west due to $\{v_1^T\}$. Near the upstream end both thermal forcing and surface damping restore the vertical shear so that waves can begin to grow farther upstream. This wave growth becomes the downstream fringe of the next wave packet.

We have also applied this analysis method to the results of a more realistic model, the idealized GCM that was briefly described in section 3.

Figures 16a–e show the fast phase-averaged variance of the meridional wind ($\{v^{*2}\}_{205}$) and eddy relative vorticity flux ($\{v^*\zeta^*\}_{205}$) at 205 mb, the heat fluxes at 205 ($\{v^*T^*\}_{205}$), and at 830 mb ($\{v^*T^*\}_{830}$), and the precipitation. The location of the packet is represented by the maximum of the $\{v^{*2}\}_{205}$ field shown in Fig. 16a. We have examined packets at every level of the model and find that the vertical structure of the packet as measured by $\{v^{*2}\}$ is nearly barotropic throughout the troposphere.

The maximum poleward heat fluxes are vertically tilted to the west (compare Figs. 16c with 16d). The maximum $\{v^*\zeta^*\}_{205}$ is located about 30 degrees to the west of the packet center so that it lies slightly to the west and equatorward of the maximum poleward heat flux at 830 mb.

Precipitation also exhibits a packetlike structure (see Fig. 16e). Most of the precipitation is concentrated in a relatively small region on the equatorward and western side of the packet. The concentration of the precipitation equatorward of the packet is expected since most of the precipitation in midlatitudes occurs along fronts that stretch equatorward from the center of the cyclones. Figure 16e implies that the precipitation starts to occur at the mature stage and persists during the decay stage of the eddies in the packets.

7. Concluding remarks

The observations from the SH indicate that the summer season, with its weaker baroclinicity, exhibits coherent packets that are very similar to those in the idealized models. In the two-level PE model, we sys-

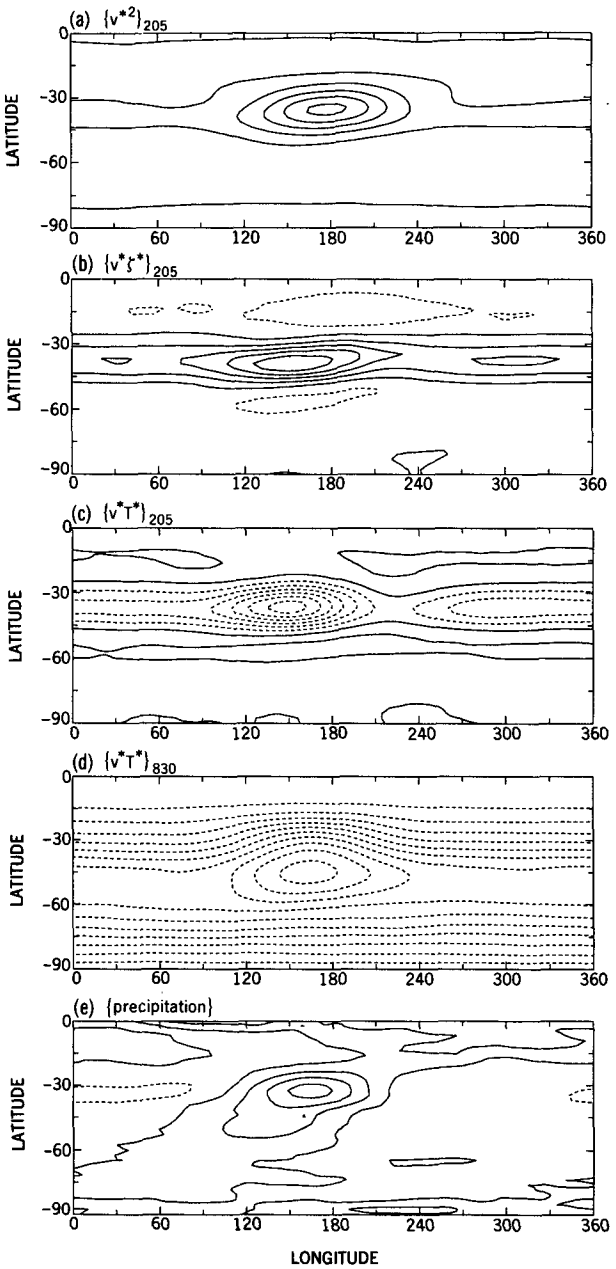

FIG. 16. Latitude–longitude contours of fast phase averaged (a) eddy meridional wind squared, (b) relative vorticity flux, (c) heat flux at 205 mb, (d) heat flux at 830 mb, and (e) precipitation. The contour intervals are (a) 60 $m^2 s^{-2}$, (b) 2×10^{-5} $m s^{-2}$, (c) 2.0 $m s^{-1}$ K, (d) 2.0 $m s^{-1}$ K, and (e) 0.03 cm day^{-1}.

tematically varied the temperature gradient between the pole and the equator to examine the effect of the supercriticality on the behavior of the baroclinic wave packet. The packets become more robust as the supercriticality of the flow is reduced. Qualitatively similar results are found in the two-layer QG model as well, in that the wave packets manifest themselves better as the nondimensional β is increased, provided that the flow is unstable enough to support finite-amplitude waves with more than two different zonal wavenumbers.

Using the two-layer QG model, we have shown that more than one packet can exist in the domain at the same time. As the length of the channel increases, with other parameters in the model being fixed, the number of packets increases in a systematic way.

While this work is not described in this paper, we have tried to obtain similar results in a simpler QG model with uniform vertical shear across the channel, rather than with a jetlike structure. In weakly unstable flows with this simpler model, coherent packets are found to evolve when two different zonal wavenumbers have comparable, small, growth rates. However, when the channel is lengthened, a wavenumber lying between these two values becomes consistent with the quantization condition due to the zonal periodicity, and this wavenumber has larger growth rate. The result is a sinusoidal, unmodulated wave train once again. The dependence of the formation of wave packets on zonal wavenumber quantization is also found in weakly unstable flows with a jetlike structure in the lower branch of solution near the linear stability boundary. In contrast, in moderately supercritical flow, the packet is much more coherent and clearly has a scale that is independent of the zonal quantization in both jet and uniform shear cases. However, the region in parameter space within which the flow is sensitive to quantization appears to be larger in the uniform shear case than in the case of an unstable jet. Also, the packets in the uniform shear case do not show any east–west asymmetric structure.

In a relatively weakly supercritical and diffusive flow, where the solution exhibits a periodic oscillation, there is a clear negative correlation between the amplitude and the half-width of the packet. This behavior is consistent with expectations based on the nonlinear Schrödinger equation (NLS). As in the solution of the NLS equation, the velocity of the packet appears to be independent of the width and amplitude of the packet. A looplike structure is observed in the scatter diagram between the amplitude and the half-width of the packet. However, at higher resolution and weaker diffusion, the flow becomes chaotic, and the pronounced negative correlation disappears, although the packet often remains remarkably coherent.

We have argued that the structure of the baroclinic waves in the packet is analogous to life cycles of unstable baroclinic waves as a function of time. Analysis of the weakly nonlinear wave packet in the two-layer QG model shows that the waves grow baroclinically in the downstream (eastern) end and decay barotropically in the upstream (western) end of the packet. Both dissipation and radiative forcing reestablish the baroclinicity of the basic flow at the western end of the packet.

The barotropic decay at the upstream end of the packet is most clearly seen in a more strongly nonlinear flow in a high-resolution model, where the potential vorticity field indicates that wave breaking occurs preferentially on the upstream side of the packet. A composite analysis of the packets in an idealized multilayer GCM is consistent with this picture of the life cycle of eddies within the packet.

The eddy "life cycle" as a function of longitude inside the packet is so similar to the temporal life cycle of an unmodulated wave that one is tempted to estimate the scale of the packet as $(C_{gx} - c)\tau$, where C_{gx} is the eddy group velocity, c the wave phase speed, and τ the time required for the zonally uniform wave train to pass through its life cycle of baroclinic growth and barotropic decay. This estimate does not work quantitatively—it overestimates the packet length by roughly a factor of 2 in the cases that we examined. Following a given high or low inside the packet, it both grows and decays faster than its counterpart in a uniform wave train. This is intuitively what one should expect, given that the growing wave is being fed by energy flux from larger disturbances upstream, and the decaying eddy is losing more energy than is received from its neighbor (Orlanski and Chang 1993). It appears that these packets have a dynamics distinct from that captured by the NLS equation. The central fact is that the unmodulated, single zonal wave train possesses a distinct asymmetric life cycle. A theory for the packet would combine this life cycle with the effect of the zonal divergence of wave energy or activity in a modulated wave train.

At least in the Southern Hemisphere, these packets may have some implications for weather forecasting. Because the packet can remain coherent despite chaotic internal dynamics, the packet envelope should be more predictable than the individual weather systems. It will be of interest to study the eddy "envelope" predictability. It may also be useful to construct the envelope of the baroclinic eddies on a routine basis by demodulation or comparable methods, for qualitative guidance as to the occurrence of periods of disturbed or stable weather.

Acknowledgments. We would like to thank Dr. Isidoro Orlanski for his helpful comments, and Peter Phillipps for integrating the idealized GCM and preparing the data for analysis. One of the authors (SL) was supported by National Science Foundation Grant ATM 8800667.

REFERENCES

Bloomfield, P., 1976: *Fourier Analysis of Time Series: An Introduction.* Wiley-Interscience, 258 pp.

Edmon, H. J., B. J. Hoskins, and M. E. McIntyre, 1980: Eliassen-Palm cross sections for the troposphere. *J. Atmos. Sci.*, **37**, 2600–2616.

Feldstein, S. B., 1991: A comparison of the weakly nonlinear instability of westerly and easterly jets in a two-layer beta-plane model. *J. Atmos. Sci.*, **48**, 1701–1717.

——, and I. M. Held, 1989: Barotropic decay of baroclinic waves in a two-layer beta-plane model. *J. Atmos. Sci.*, **46**, 3416–3430.

Fraedrich, K., and M. Lutz, 1987: A modified time–longitude diagram applied to 500 mb height along 50 degrees north and south. *Tellus*, **39A**, 25–32.

Gordon, C. T., and W. F. Stern, 1982: A description of the GFDL global spectral model. *Mon. Wea. Rev.*, **110**, 625–644.

Hendon, H. H., and D. L. Hartmann, 1985: Variability in a nonlinear model of the atmosphere with zonally symmetric forcings. *J. Atmos. Sci.*, **42**, 2783–2797.

Hide, R., P. J. Mason, and R. A. Plumb, 1977: Thermal convection in a rotating fluid subject to a horizontal temperature gradient: Spatial and temporal characteristics of fully developed baroclinic waves. *J. Atmos. Sci.*, **34**, 930–950.

Hovmöller, E., 1949: The trough-and-ridge diagram. *Tellus*, **1**, 62–66.

Joung, C. H., and M. H. Hitchman, 1982: On the role of successive development in east Asian polar air outbreaks. *Mon. Wea. Rev.*, **110**, 1224–1237.

Lee, S., and I. M. Held, 1991: Subcritical instability and hysteresis in a two-layer model. *J. Atmos. Sci.*, **48**, 1071–1077.

Manabe, S., D. G. Hahn, and J. L. Holloway, 1979: Climate simulation with GFDL spectral models of the atmosphere. GARP Publ. Ser. No. 22, WMO, Geneva.

Mason, P. J., 1975: Baroclinic waves in a container with sloping endwalls. *Phil. Trans. Roy. Soc. London*, **A278**, 397–445.

Moroz, I. M., 1981: Slowly modulated baroclinic waves in a three-layer model. *J. Atmos. Sci.*, **38**, 600–608.

——, and J. Brindley, 1981: Evolution of baroclinic wave packets in a flow with continuous shear and stratification. *Proc. Roy. Soc. London*, **A377**, 379–404.

——, and ——, 1984: Nonlinear amplitude evolution of baroclinic wave trains and wave packets. *SIAM*, **70**, 21–62.

Namias, J., and P. F. Clapp, 1944: Studies of the motion and development of long waves in the westerlies. *J. Meteor.*, **1**, 57–77.

Orlanski, I., and J. Katzfey, 1991: The life cycle of a cyclone wave in the Southern Hemisphere. Part I: Eddy energy budget. *J. Atmos. Sci.*, **48**, 1972–1998.

——, and K. M. Chang, 1993: Ageostrophic geopotential fluxes in downstream and upstream development of baroclinic waves. *J. Atmos. Sci.*, **50**, 212–225.

Pedlosky, J., 1972: Finite-amplitude baroclinic wave packets. *J. Atmos. Sci.*, **29**, 680–686.

Randel, W. J., and J. L. Stanford, 1985: The observed life-cycle of a baroclinic instability. *J. Atmos. Sci.*, **42**, 1364–1373.

——, and I. M. Held, 1991: Phase speed spectra of transient eddy fluxes and critical layer absorption. *J. Atmos. Sci.*, **48**, 688–697.

Simmons, A. J., and B. J. Hoskins, 1978: The life-cycles of nonlinear baroclinic waves. *J. Atmos. Sci.*, **42**, 1364–1373.

——, and ——, 1979: The downstream and upstream development of unstable baroclinic waves. *J. Atmos. Sci.*, **36**, 1239–1254.

Trenberth, K. E., 1982: Seasonality in Southern Hemisphere eddy statistics at 500 mb. *J. Atmos. Sci.*, **39**, 2507–2520.

——, 1986: An assessment of the impact of transient eddies on the zonal flow during a blocking episode using localized Eliassen–Palm flux diagnostics. *J. Atmos. Sci.*, **43**, 2070–2087.

van Loon, H., 1965: A climatological study of the atmospheric circulation in the Southern Hemisphere during the IGY. Part I: July 1957–31 March 1958. *J. Appl. Meteor.*, **4**, 479–491.

Whitham, G. B., 1974: *Linear and Nonlinear Waves.* Wiley-Interscience, 636 pp.